### Title

Computational prediction of Mg-isotope fractionation between aqueous [Mg(OH2)6]2+ and brucite




### Authors

Colla, Christopher A
Casey, William H
Ohlin, C André



### Publication Date

2018-04-01

### DOI

10.1016/j.gca.2018.02.005

Peer reviewed

Available online at www.sciencedirect.com

ScienceDirect

Geochimica et Cosmochimica Acta 227 (2018) 64–74

Geochimica et Cosmochimica Acta

www.elsevier.com/locate/gca

# Computational prediction of Mg-isotope fractionation between aqueous $[Mg(OH_2)_6]^{2+}$ and brucite

Christopher A. Colla [a,*], William H. Casey [a,b], C. André Ohlin [c,*]

[a] Department of Earth and Planetary Sciences, University of California, 1 Shields Avenue, Davis, CA 95616, USA
[b] Department of Chemistry, University of California, 1 Shields Avenue, Davis, CA 95616, USA
[c] Department of Chemistry, Faculty of Science and Technology, Umeå University, Sweden

Received 4 August 2017; accepted in revised form 2 February 2018; available online 14 February 2018

**Abstract**

The fractionation factor in the magnesium-isotope fractionation between aqueous solutions of magnesium and brucite changes sign with increasing temperature, as uncovered by recent experiments. To understand this behavior, the Reduced Partition Function Ratios and isotopic fractionation factors ($\Delta^{26/24}Mg_{brucite\text{-}Mg(aq)}$) are calculated using molecular models of aqueous $[Mg(OH_2)_6]^{2+}$ and the mineral brucite at increasing levels of density functional theory. The calculations were carried out on the $[Mg(OH_2)_6]^{2+}{\cdot}12H_2O$ cluster, along with different Pauling-bond-strength-conserving models of the mineral lattice of brucite. Three conclusions were reached: (i) all levels of theory overestimate ⟨Mg—O⟩ bond distances in the aqua ion complex relative to Tutton's salts; (ii) the calculations predict that brucite at 298.15 K is always enriched in the heavy isotope, in contrast with experimental observations; (iii) the temperature dependencies of Wimpenny et al. (2014) and Li et al. (2014) could only be achieved by fixing the ⟨Mg—O⟩ bond distances in the $[Mg(OH_2)_6]^{2+}{\cdot}12H_2O$ cluster to values close to those observed in crystals that trap the hydrated ion.


*Keywords:* Mg-isotopes; Isotope fractionation; Brucite; Density functional theory; Electronic structure

## 1. INTRODUCTION

The theoretical and experimental understanding of low-temperature fractionation of stable metal isotopes has advanced considerably over the last two decades (see review by Schauble et al., 2009). The stable isotopes of magnesium, calcium and iron are particularly important because of their natural abundance in minerals, and because of their use in paleoenvironmental reconstruction (see Anbar and Rouxel, 2007). For light metals such as these, the equilibrium fractionation is predominantly controlled by the relative masses of the isotopomers via their influence on the vibrational frequencies of the molecule, or of the metal-ligand bond in the solid. Coordination environments with heavier isotopes vibrate at lower frequencies than those with lighter isotopes. The isotopic fractionation also correlates with bond strength because coordination environments with strong, short bonds select for heavy isotopes. Such mass-dependent isotopic fractionation can be treated theoretically because it is described by calculable vibrational frequencies.

Here we use electronic-structure calculations and density functional theory (DFT) to compute the isotopic fractionation between aqueous $[Mg(OH_2)_6]^{2+}$ and the mineral brucite, $Mg(OH)_2$, building on previous low- and high-temperature experimental, and theoretical work (Black et al., 2007; Rustad et al., 2010; Schauble, 2011; Young et al., 2015; Wu et al., 2015; Pinilla et al., 2015). The magnesium-isotope system is well suited for simulation because, unlike iron, it has a fixed valence state under

* Corresponding authors.
*E-mail addresses:* cacolla@ucdavis.edu (C.A. Colla), andre.ohlin@umu.se (C.A. Ohlin).

https://doi.org/10.1016/j.gca.2018.02.005
0016-7037/

aqueous environmental conditions and because relativistic effects are small as the nucleus is so light.

Furthermore, aqueous Mg(II) ions have a fixed, well-known coordination number, unlike aqueous Ca(II) and Li(I), in addition to a simple hydrolysis chemistry (see Colla et al., 2013; Wimpenny et al., 2015). The aqueous magnesium ion is exclusively octahedral as $[Mg(OH_2)_6]^{2+}$ (see review by Ohtaki and Radnai, 1993). Evidence includes X-ray diffraction studies on a variety of magnesium derivatives of Tutton's salts, which have the general stoichiometry $X_2Mg(YO_4)\cdot 6H_2O$, where X is a univalent cation such as potassium, and Y is either selenium or sulfur, with the $[Mg(OH_2)_6]^{2+}$ moiety trapped in the crystal lattice (Richens, 1997). Thus the ⟨Mg—O⟩ bond lengths of $[Mg(OH_2)_6]^{2+}$ in these salts are well known experimentally.

The need for geochemists to understand isotope exchange between aqueous Mg(II) complexes and brucite is particularly compelling, as the brucitic $Mg(OH)_2$ octahedral layer is a fundamental building block for minerals such as talc, chrysotile, chlorite, antigorite and vermiculite. The fractionation of magnesium isotopes between aqueous solutions and brucite has recently been experimentally determined in two studies, which when combined indicate a strong temperature dependence (Li et al., 2014; Wimpenny et al., 2014). Li et al. (2014) pointed out that a *reversal* from positive to negative fractionation factors with temperature decreases was suggested by their data, which was supported by the observations of Wimpenny et al. (2014) (Fig. 1). While temperature reversals have been observed in C-, H- and O-isotope systems, they are generally uncommon and have never before been observed in heavier and non-traditional stable-isotope systems (Li et al., 2014).

Wimpenny et al. (2014) synthesized brucite by adding a solution of 0.1 M $MgCl_2$ to a 0.1 M solution of NaOH, and isolated the solution in an argon atmosphere to avoid the uptake of $CO_2$ gas, which would result in the precipitation

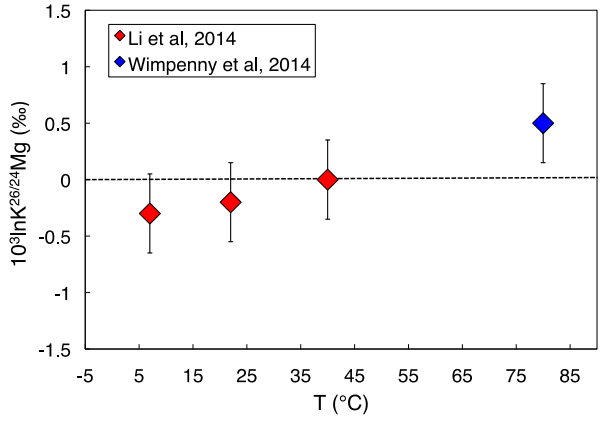


Fig. 1. A plot of $10^3 \ln K^{26/24}Mg$ versus temperature from the combined experimental data of Li et al. (2014) and Wimpenny et al. (2014). Error bars indicate one standard deviation of the mean. The plot depicts a clear decrease in the isotopic equilibrium constant as temperature decreases as measured by two separate studies, indicated by red and blue. (For interpretation of the references to colour in this figure legend, the reader is referred to the web version of this article.)

of magnesite. Upon mixing of $MgCl_2$ into NaOH, a white precipitate formed immediately. The resulting solution had a near neutral pH at room temperature, and the solution-precipitate mixture was reacted in an oven at 80 °C. Solids and solutions were sampled every other day for two weeks. Powder X-ray diffraction confirmed the existence of pure brucite with no carbonate impurities. The low-temperature experiments of Li et al. (2014) synthesized brucite via the reaction of MgO powder with $H_2O$. MgO was added to an aqueous solution of 0.2 M HCl, and reacted at three different tempertures, 7 °C, 22 °C, and 40 °C. In this reaction, HCl liberates Mg(II) from MgO, therefore exchanging aqueous Mg(II) with freshly precipitated brucite from the reaction of MgO with $H_2O$. Samples were collected after 100 days and X-ray diffraction analysis confirmed the resulting solid to be brucite with no MgO or magnesite impurities.

Isotopic equilibrium was apparently attained in the study of Wimpenny et al. (2014) as steady state was reported after ten days, with a $\Delta^{26/24}Mg_{solid\text{-}solution}$ value of 0.5‰, which was observed by the end of the experiment at day 323. They also reversed the experimental solution by diluting the solution and observed that the $\Delta^{26/24}Mg_{solid\text{-}solution}$ of 0.5‰ was again attained after a few days (compare Figs. 4 and 5 in Wimpenny et al. 2014). The reversed dissolution experiments were not nearly as comprehensive as the growth experiments that lasted 323 days, but seem to rule out control by kinetic fractionation. Li et al. (2014) speculate that a kinetic isotope effect could exist and cite evidence from studies of Mg isotope fractionation in calcite as a function of crystallization rate (Immenhauser et al., 2010; Mavromatis et al., 2013; Li et al., 2014). Mavromatis et al. (2013) argue that Mg-isotopic equilibrium can be reached at calcite crystallization rates below $10^{-8.5}$ mol/m$^2$/s because desolvation of the Mg(II) aqua ion has negligible kinetic isotope effects (Mavromatis et al., 2013; Li et al., 2014), and this step is presumed to be the key step in kinetic fractionation.

## 2. METHODS

### 2.1. Isotope conventions

The exchange of the heavy ($^{26}$Mg) and light ($^{24}$Mg) isotopes between two phases or in this case $Mg^{2+}(aq)$ and brucite $[Mg(OH)_2]$ can be written as in Eq. (1),

$$^{24}Mg(OH)_2(s) + {}^{26}Mg^{2+}(aq) = {}^{26}Mg(OH)_2(s) + {}^{24}Mg^{2+}(aq) \quad (1)$$

where $(aq)$ indicates the fully aquated ion (i.e., $[Mg(OH_2)_6]^{2+}$) in the solution phase and $(s)$ indicates the solid phase. The $\delta$ notation is used to report the isotopic composition of either a solid or solution where $\delta^{26/24}Mg_i$ is the isotopic variation with respect to a standard in units of per mil (‰) (Eq. (2)).

$$\delta^{26/24}Mg_i = 1000\left(\frac{\left(\frac{^{26}Mg}{^{24}Mg}\right)_i}{\left(\frac{^{26}Mg}{^{24}Mg}\right)_{std}} - 1\right) \quad (2)$$

The numerator can be the isotopic composition of either the solid or the ion, while the denominator is the isotopic composition of a standard. The $\Delta^{26/24}Mg_{solid\text{-}solution}$ isotopic fractionation factor can then be calculated as in Eq. (3):

$$\Delta^{26/24}Mg_{solid\text{-}solution} = \delta^{26/24}Mg_{solid} - \delta^{26/24}Mg_{solution} \quad (3)$$

When $\Delta^{26/24}Mg_{solid\text{-}solution}$ values are positive, the solid phase is enriched in the heavy isotope while negative values of $\Delta^{26/24}Mg_{solid\text{-}solution}$ indicate that the solid is depleted in the heavy isotope. The $\Delta^{26/24}Mg_{solid\text{-}solution}$ isotope fractionation factor is approximately equal to the equilibrium constant for isotope exchange as derived by Bigeleisen and Mayer (1947) (Eq. (4)).

$$\Delta^{26/24}Mg_{solid\text{-}solution} \approx 10^3 \cdot \ln K^{26/24}Mg_{solid\text{-}solution} \quad (4)$$

### 2.2. Electronic-structure methods

We here employ the methods of Rustad et al. (2008), Rustad and Dixon (2009), Rustad et al. (2010) and use density functional theory to compute the harmonic vibrational frequencies, reduced partition function ratios (RPFRs) and the expected equilibrium isotopic fractionation factors between $[Mg(OH_2)_6]^{2+}$ and the mineral brucite. Computations were carried out with Gaussian 09, revision E.01 (Frisch et al., 2013). Clusters representing the aqueous and mineral environments were structurally optimized as described below and the frequencies were computed with the following exchange-correlation (XC) functionals: BP86 (Perdew, 1986; Becke, 1988), PBE (Perdew et al., 1996a,b), B3PW91 (Becke, 1993), PBE0 (Adamo and Barone, 1999), LC-ωPBE (Vydrov and Scuseria, 2006) and ωB97XD (Chai and Head-Gordon, 2008). Different combinations of basis sets, XCs and solvation models were explored to identify a model chemistry that gave consistent results with a computational performance that allowed for larger cluster fragments to be investigated.

Much of the previous work employed clusters in the gas phase to approximate ions, or has used clusters that were embedded in implicit continuum solvent models such as PCM (Tomasi et al., 2005) or COSMO (Klamt and Schuurman (1993)). In a particularly exhaustive study, Rustad et al. (2010) pointed out that aqueous cluster models with up to thirty-three explicit water molecules are necessary to reach converged RPFR values for cations in the gas phase, while demonstrating that similar convergence can be achieved by embedding ions with as few as eighteen water molecules in a dielectric medium. Both the eighteen and thirty-three water molecule clusters have an explicit second shell (Rustad and Dixon, 2009; Rustad et al., 2010). Here we adopt the eighteen-water cluster geometry that is embedded in a continuum dielectric to compute RPFRs, so that the aqueous Mg(II) species is represented by a $[Mg(OH_2)_6]^{2+}$ ion in a second shell of twelve water molecules (Fig. 2a). The positions of the atoms of the second outer shell of water molecules were fixed and only the positions of the atoms in the $[Mg(OH_2)_6]^{2+}$ core were computationally optimized (Rustad et al., 2010). We will refer to the former atom set as 'frozen' atoms, and the rest as 'active' atoms. Before the DFT optimization, the $[Mg(OH_2)_6]^{2+}\cdot 12H_2O$ model was reacted using a Car-Parinello Molecular Dynamics simulation (CPMD), as described in Rustad et al. (2010), to achieve an approximately optimized structure.

The crystal information file for brucite was taken from the work of Zigan and Rothbauer (1967), who determined the complete structure with neutron diffraction. The brucite model was constructed by excising a fragment from the crystal structure of brucite and adding link atoms at a distance of 1 Å from the nearest oxygen, with charges adjusted to the charge divided by the coordination number of the oxygen ($2^+/6$) so that the overall fragment cluster has a neutral charge. This approach has previously been referred to as the Pauling Bond Strength (PBS) conserving termination method (see e.g. Rustad et al., 2010). The use of the PBS-conserving termination method creates a neutral, autocompensated cluster (Rustad et al., 2008).

A wide range of combinations of basis sets for the different atoms in the cluster were explored, with the goal of gauging the importance of using large basis sets on the frozen atoms, as well as on the active ones. In most cases we compared the use of large (e.g. triple-zeta) basis sets on all atoms with the use of double-zeta basis sets for the frozen atoms and triple-zeta basis sets on the active ones, i.e. the core $[Mg(OH_2)_6]^{2+}$ ion. Basis sets with diffuse functions, in addition to polarization functions, were generally applied to O and H atoms of the core and can be necessary for modeling hydrogen bonding accurately (Rustad et al., 2010). Models with diffuse functions are used to treat weak interactions like hydrogen bonding because the functions allow for electrons to be further away from the nucleus, describing electrons in weakly bound orbitals more accurately (Papajak and Truhlar, 2010).

The brucite model was first constructed using the crystal structure of brucite. The active $[Mg(OH)_6]^{4-}$ core was then optimized with the outer atoms frozen, and by adjusting the charge of the terminal link atoms to yield a neutral cluster, as outlined above.

Some of the advantages to using the embedded-cluster method for calculating vibrational frequencies and equilibrium isotopic fractionations, include: (i) hybrid functionals can be used, which employ some amount of exact exchange. The use of exact exchange in plane-wave DFT is computationally expensive to implement (Rustad and Dixon, 2009). (ii) It is also advantageous to use the same electronic structure method on both the aqua ion and mineral environment to acquire the greatest amount of error cancellation (Rustad et al., 2010). Rustad and Dixon (2009) point out that one disadvantage to using the embedded cluster method is the lack of phonon contributions to the fractionation because, in reality, one is conducting a gas phase calculation on a discrete group of atoms, unlike a system with periodic boundaries. We chose this approach because adopting the embedded-cluster method was the most computationally efficient and inexpensive way to compute isotopic fractionation.

To better understand the trend of the fractionation factor with temperature, the vibrational frequencies for the $[Mg(OH_2)_6]^{2+}$ ion in the minerals epsomite and picromerite were computed. In general, hydrate phases that incorporate

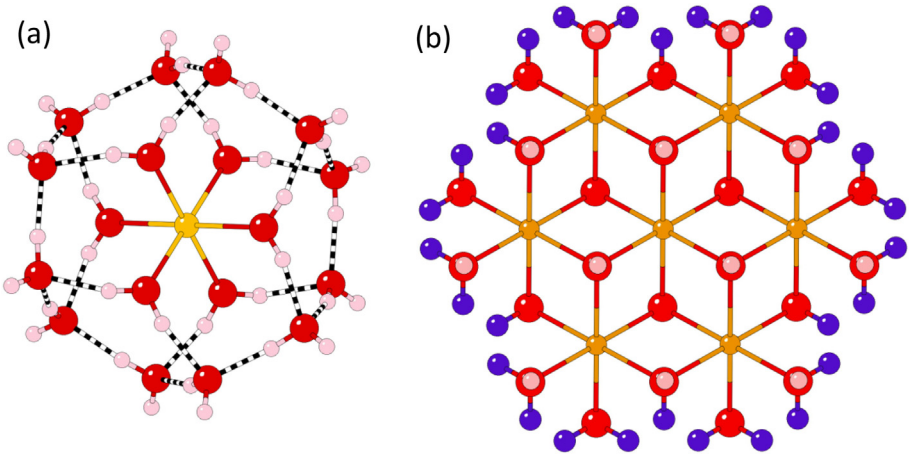


Fig. 2. Optimized molecular models that were used to represent the brucite mineral and aqueous environments. (a) A representation of the $[Mg(OH_2)_6]^{2+}$ aqueous environment, where dashed bonds indicate hydrogen bonding. (b) A representation of the brucite mineral environment. Yellow spheres are magnesium atoms, red spheres are oxygen atoms, light pink spheres represent hydrogen atoms and purple spheres are link atoms that exist only to neutralize the unsatisfied charge. (For interpretation of the references to colour in this figure legend, the reader is referred to the web version of this article.)

the metal aqua ion are good representations of the moiety in aqueous solutions (Richens, 1997). While not optimizing the $[Mg(OH_2)_6]^{2+}$ ion prior to computing the vibrational frequencies leads to imaginary frequencies, and thus are to be rejected at face value, the similarity of the resulting RPFR led us to include them to compare with fully optimized calculations. The vibrational frequencies for the $[Mg(OH_2)_6]^{2+}$ ions were computed with the PBE0 exchange-correlation functional and the cc-pVTZ basis set on all atoms.

To specifically investigate the effect of ⟨Mg—O⟩ bond lengths on the $[Mg(OH_2)_6]^{2+}\cdot 12H_2O$ RPFR, ⟨Mg—O⟩ bond distances were fixed at various lengths as the rest of the structure was optimized. The geometries were then used to compute the vibrational frequencies and corresponding RPFRs. The calculations were carried out using the PBE0 exchange-correlation functional with the cc-pVTZ basis set on all atoms and PCM as the implicit solvation model (PBE0/cc-pVTZ + PCM). In order to fix ⟨Mg—O⟩ bond distances, a z-matrix was built and the ⟨Mg—O⟩ distances were manually set to the chosen values (e.g. 2.050, 2.065, 2.070, 2.075 or 2.080 Å) in each calculation.

In order to represent the extended crystalline lattice of the mineral brucite, and to assess the effect of cluster size on the RPFR (see Rustad et al., 2010), three cluster models were created according to the PBS method (Rustad et al., 2008).

Three clusters of varying sizes were cut from the crystal structure of brucite in one of three ways: (i) model I incorporates the core $[Mg(OH)_6]^{4-}$ and the six Mg octahedra surrounding the core (Fig. 2b); (ii) model II adds a third shell of Mg octahedra (SI-Fig. 1a); (iii) model III consists of three stacked layers of the structures made in Model I (SI-Fig. 1b). All Mg-centered octahedra – a total of seven in Model I and nineteen in Model II – were included in the cluster. The harmonic frequencies for the heavy $^{26}Mg$ (25.98259292 amu) and light $^{24}Mg$ (23.985041700 amu) isotopes were calculated by first generating a matrix of force constants using Gaussian, and then computing the frequencies with an auxiliary code (See Supplemental Information).

In all cases the structure was first geometrically optimized, and the normal modes calculated for the light and heavy Mg isotopes. The corresponding frequencies are then used to calculate the RPFR, denoted as $\beta$ here, for the solid and aqueous species (Rustad et al., 2010). In the harmonic approximation, the RPFR for the heavy and light isotope is defined in Eq. (5), where $Q_{(h,l)}$ are the vibrational partition coefficients for the heavy and light isotopes and $u_{(h,l)i} = hc\omega_{(h,l)}/k_BT$ (Urey, 1947), and where $h$ is Planck's constant, $c$ is the speed of light, $\omega$ is the vibrational frequency of the heavy or light isotope, $k_B$ is Boltzman's constant and $T$ is the absolute temperature in Kelvin. The product is taken over all vibrational terms (Eq. (5); Urey, 1947).

$$\beta = \left(\frac{Q_h}{Q_l}\right) = \prod_i^{3N} \frac{u_{h_i}}{u_{l_i}} \frac{e^{-u_{h_i}/2}}{1-e^{-u_{h_i}}} \frac{1-e^{-u_{l_i}}}{e^{-u_{l_i}/2}} \tag{5}$$

The isotope-fractionation factor, Δ, is then calculated via Eq. (6), which is related to the equilibrium constant for exchange in Eq. (4).

$$\Delta^{26/24}Mg_{brucite-Mg^{2+}(aq)} \approx \ln\left(\frac{\beta_{brucite}}{\beta_{Mg^{2+}(aq)}}\right)10^3 \tag{6}$$

## 3. RESULTS

Brucite is consistently predicted to be isotopically heavier than the aqueous $[Mg(OH_2)_6]^{2+}$ ion in these models (Table 9). Furthermore, computations using small basis sets compare well to results using much more expensive levels of theory. The results of the electronic-structure calculations are summarized in Tables 1–3 where the RPFRs of the eighteen-water cluster of Mg(II) are reported. We observed that the RPFR values converged as the number of basis

Table 1
Reduced partition function ratios for the $[Mg(OH_2)_6]^{2+}\cdot 12H_2O$ cluster using the BP86 and PBE exchange-correlation functionals at 298.15 K and different combinations of basis sets on the active atoms. Pople-style basis set combinations used 6-31G* basis set on second shell waters.

| XC/basis set/solvation | $\beta$(RPFR) |
|---|---|
| *BP86* | |
| 6-31G*(O, H, Mg) | 1.024615 |
| 6-31G*(O, H, Mg)/PCM | 1.021953 |
| 6-311++G(2d, 2p)(O, H)/6-311G(Mg) | 1.022480 |
| 6-311++G(2d, 2p)(O, H)/6-311G(Mg)/PCM | 1.022481 |
| *PBE* | |
| 6-311++G(2d, 2p)(O, H)/6-311G(Mg) | 1.021972 |
| 6-311++G(2d, 2p)(O, H)/6-311G(Mg)/PCM | 1.018945 |

functions increased (Fig. 3). Included in Fig. 3 are the calculations of Schott et al. (2016). The position of their data in the compilation suggests that their higher RPFR values maybe due to the smaller basis sets that they used in their study, and the lack of a second explicit solvation shell. This convergence also allowed us to select a method that combined computational expediency with accuracy. For example, the combination of PBE0/cc-pVTZ (all atoms) and PCM gives an RPFR of 1.022559 while using PBE0/6-311++G(2d, 2p) on O and H of the first shell and cc-pVTZ on Mg and the second-shell waters achieved an RPFR that is only $1 \cdot 10^{-4}$ lower than that more expensive calculation. By using cc-pVTZ on Mg, O and H of the first shell and applying cc-pVDZ to the twelve second-shell waters, we can achieve an RPFR that is only $1.1 \cdot 10^{-4}$ lower, but has half the number of basis functions of the larger calculation.

These calculations with smaller basis set/functional combinations compare well to results using the much larger aug-cc-pVTZ basis set on Mg, O, and H of the core ion, with the second shell treated using the double-zeta cc-pVDZ basis set. The RPFR values from the aug-cc-pVTZ calculations were approximately $2 \cdot 10^{-4}$ lower than those calculated using cc-pVTZ on all atoms, which we consider to be acceptably close. Similarly, the combination of PBE0, def2-TZVP on the core atoms and def2-SVP on the second shell in both the brucite and $[Mg(OH_2)_6]^{2+}\cdot 12H_2O$ model yielded a result that agrees well with the computations at PBE0/cc-pVTZ on all atoms. The def2 basis sets are effective core potential (ECP) basis sets and it was of particular interest to evaluate these basis sets with future, transition-metal-containing systems in mind.

Table 3
Reduced partition function ratios for the $[Mg(OH_2)_6]^{2+}\cdot 12H_2O$ cluster using the LC-ωPBE and ωB97XD exchange-correlation functionals at 298.15 K and different basis set combinations on the active atoms.

| XC/basis set/solvation | $\beta$(RPFR) |
|---|---|
| *LC-ωPBE* | |
| cc-pVTZ(O, H, Mg)/cc-pVDZ(2nd Shell)/PCM | 1.022822 |
| *ωB97XD* | |
| cc-pVTZ(O, H, Mg)/cc-pVDZ(2nd Shell)/PCM | 1.023123 |

The similarity of the results obtained with the combination of def2-TZVP/def2-SVP with those from the cc-pVTZ/cc-pVDZ combination is important and suggests that the reactivity trend is robust, and diffuse forms of the ECP basis sets were not further investigated. The long-range-corrected functionals LC-ωPBE and ωB97XD give RPFRs that are slightly higher than those obtained at the PBE0/cc-pVTZ with PCM level of theory (Table 3).

The results of the electronic-structure calculations for the brucite PBS model (Fig. 2b) are summarized in Tables 6–8. Similar to the RPFR calculations for the aqueous $[Mg(OH_2)_6]^{2+}\cdot 12H_2O$ model, PBE0/cc-pVTZ with PCM was used as a reference because it has the highest number of basis functions and gives an RPFR of 1.025775 (Fig. 4). As was observed for the $[Mg(OH_2)_6]^{2+}\cdot 12H_2O$ model, the combination of triple- and double-zeta basis functions along with the PBE0 exchange-correlation functional generally gave similar results to a calculation using cc-pVTZ for all atoms (Table 7).

Table 2
Reduced partition function ratios for the $[Mg(OH_2)_6]^{2+}\cdot 12H_2O$ cluster using the B3PW91 and PBE0 exchange-correlation functionals at 298.15 K and different basis set combinations on the active atoms. Pople basis sets used 6-31G* basis set on second shell waters.

| XC/basis set/solvation | $\beta$(RPFR) |
|---|---|
| *B3PW91* | |
| 6-311++G(2d, 2p)(O, H)/6-311G(Mg) | 1.023714 |
| 6-311++G(2d, 2p)(O, H)/6-311G(Mg)/PCM | 1.020256 |
| *PBE0* | |
| 6-311++G(2d, 2p)(O, H)/6-311G(Mg) | 1.023721 |
| 6-311++G(2d, 2p)(O, H)/6-311G(Mg)/PCM | 1.020972 |
| cc-pVTZ(O, H, Mg)/cc-pVDZ(2nd Shell)/PCM | 1.022450 |
| cc-pVTZ(O, H, Mg)/cc-pVDZ(2nd Shell)/CPCM | 1.021792 |
| cc-pVDZ(O, H, Mg)/PCM | 1.025066 |
| cc-pVTZ(O, H, Mg)/PCM | 1.022559 |
| def2-TZVP(O, H, Mg)/def2-SVP(2nd Shell)/PCM | 1.022466 |
| aug-cc-pVTZ(O, H, Mg)/cc-pVDZ(2nd Shell)/PCM | 1.022339 |
| aug-cc-pVTZ(O, H)/cc-pVTZ(Mg)/cc-pVDZ(2nd Shell)/PCM | 1.022367 |
| 6-311++G(2d, 2p)(O, H)/cc-pVTZ(Mg, 2nd Shell)/PCM | 1.022458 |

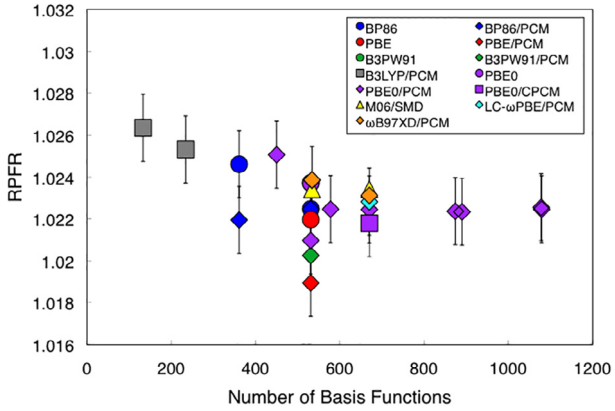


Fig. 3. Convergence of the $[Mg(OH_2)_6]^{2+}\cdot 12H_2O$ RPFR as a function of the number of basis functions from various basis set combinations and solvation models used in this study and calculations reproduced from the study of Schott et al. (2016) (grey squares). Error bars indicate one standard deviation of the range. For a list of basis set combinations and corresponding number of basis functions used in this figure, the reader is referred to Table SI-4.

All of the above calculations exhibited a significant discrepancy between the ⟨Mg—O⟩ bond lengths calculated for the $[Mg(OH_2)_6]^{2+}\cdot 12H_2O$ model and those measured in crystal hydrates. The average calculated ⟨Mg—O⟩ bond distances for the $[Mg(OH_2)_6]^{2+}\cdot 12H_2O$ cluster are compared to the average measured bond distances measured in Mg-hydrate salts in Table 4. In Table 5 ⟨Mg—O⟩ bond distances in aqua ions from previous studies are compared to results from this study, along with the corresponding RPFR values. The GGA functionals (e.g. BP86) typically overestimate bond distances, while hybrid functionals (e.g. B3LYP) give better results. Uncompensated negative charges lead to expansion as well. Big basis sets commonly especially with diffuse functions, tend to give larger structures. Although the PBE0 functional is generally found not to overestimate bond distances when compared to measurements, we find the discrepancies to be considerable for the magnesium ions. Bond lengths in the $[Mg(OH_2)_6]^{2+}$ ion here, on average are overestimated by 0.044 Å, which introduces a large change in the RPFR (see Fig. 6). The ⟨Mg—O⟩ bond distances obtained using the pure DFT BP86 exchange-correlation functional agree best with those in the Tutton's salts, but the functional still overestimates the bond distance by ~0.02 Å, consistent with previous observations (Rustad et al., 2010).

In contrast, the bond distances calculated from DFT for solid brucite agree well with measured ⟨Mg—O⟩ bond distances for the mineral (Table 4), but this result is to be expected as the system is so heavily constrained. Whereas the aqueous ion is connected to the frozen atoms only via weak hydrogen bonds, in the brucite model the active core is connected via strong covalent bonds, which severely restrict the movement of atoms during structural optimization. The average ⟨Mg—O⟩ bond-length predictions for brucite are 0.003 Å longer than those measured in neutron-diffraction experiments (Zigan and Rothbauer, 1967). All bond distances as a function of the exchange-correlation functional are tabulated in Tables SI-1 and SI-2 of the Supplemental Information.

The effect of the size of the mineral lattice on the calculation results was also explored, and found to be negligible. In particular, increasing the number of $Mg(O)_6$ octahedra in the 001 plane at PBE0/6-311++G(2d, 2p) on O and H, with the 6-311G basis set on the Mg of the core thirteen atoms, and 6-31G* on the rest of the lattice (Model II) gives an almost identical RPFR to Model I.

In summary, the computed Mg-isotope fractionation factors ($\Delta^{26/24}Mg_{solid\text{-}solution}$) indicate that brucite should always be enriched in $^{26}Mg$ by +3 to +7‰ at 298.15 K (Table 9). The calculations also indicate that brucite should

Table 4
Calculated average ⟨Mg—O⟩ bond lengths in Ångströms for both $[Mg(OH_2)_6]^{2+}\cdot 12H_2O$ and brucite. $[Mg(OH_2)_6]^{2+}\cdot 12H_2O$ is compared to the average ⟨Mg—O⟩ bond distances in epsomite and the brucite model is compared to the average ⟨Mg—O⟩ bond distances in the mineral measured by neutron diffraction.

| Calculated (Å) | Measured (Å) |
|---|---|
| *$[Mg(OH_2)_6]^{2+}\cdot 12H_2O$* | |
| 2.111 | 2.065[a] |
| *Brucite* | |
| 2.100 | 2.097[b] |

[a] Bauer (1964).
[b] Zigan and Rothbauer (1967).

Table 5
Calculated RPFRs in per mil, and ⟨Mg—O⟩ bond lengths in Ångströms for the $[Mg(OH_2)_6]^{2+}$ ion in this study and others.

| | Calculated ⟨Mg—O⟩ (Å) | RPFR[a] |
|---|---|---|
| Rustad et al. (2010) | 2.096 | 23.66 |
| Pinilla et al. (2015) | 2.090 | 23.30 |
| Schauble (2011) | 2.100[b] | 25.52[c] |
| This study | 2.111[d] | 22.31 |
| This study | 2.050[e] | 27.61 |

[a] Calculated as $10^3\ln(\beta)$ at 298.15 K.
[b] Average ⟨Mg—O⟩ bond length from Schauble (2011).
[c] Mean value of hexahydrate ion in salts, Schauble (2011).
[d] Average ⟨Mg—O⟩ bond length for all calculations in this study.
[e] Fixed ⟨Mg—O⟩ bond length in this study.

Table 6
Reduced partition function ratios for the brucite cluster using the BP86 and PBE exchange-correlation functionals at 298.15 K. Pople basis sets used 6-31G* basis set on the second shell.

| XC/basis set/solvation | $\beta$(RPFR) |
|---|---|
| *BP86* | |
| 6-31G*(O, H, Mg) | 1.029552 |
| 6-31G*(O, H, Mg)/PCM | 1.027653 |
| 6-311++G(2d, 2p)(O, H)/6-311G(Mg) | 1.028122 |
| 6-311++G(2d, 2p)(O, H)/6-311G(Mg)/PCM | 1.028866 |
| *PBE* | |
| 6-311++G(2d, 2p)(O, H)/6-311G(Mg) | 1.027473 |
| 6-311++G(2d, 2p)(O, H)/6-311G(Mg)/PCM | 1.026318 |

Table 7
Reduced partition function ratios for the brucite cluster using the B3PW91 and PBE0 exchange-correlation functionals at 298.15 K. Pople basis sets used 6-31G* basis set on the second shell.

| XC/basis set/solvation | $\beta$(RPFR) |
|---|---|
| *B3PW91* | |
| 6-311++G(2d, 2p)(O, H)/6-311G(Mg) | 1.028724 |
| 6-311++G(2d, 2p)(O, H)/6-311G(Mg)/PCM | 1.026653 |
| *PBE0* | |
| 6-311++G(2d, 2p)(O, H)/6-311G(Mg) | 1.028900 |
| 6-311++G(2d, 2p)(O, H)/6-311G(Mg)/PCM | 1.026888 |
| cc-pVTZ(O, H, Mg)/cc-pVDZ(2nd Shell)/PCM | 1.028215 |
| cc-pVTZ(O, H, Mg)/cc-pVDZ(2nd Shell)/CPCM | 1.026376 |
| cc-pVDZ(O, H, Mg)/PCM | 1.025947 |
| cc-pVTZ(O, H, Mg)/PCM | 1.025775 |
| def2-TZVP(O, H, Mg)/def2-SVP(2nd Shell)/PCM | 1.026329 |
| aug-cc-pVTZ(O, H, Mg)/cc-pVDZ(2nd Shell)/PCM | 1.025727 |
| aug-cc-pVTZ(O, H)/cc-pVTZ(Mg)/cc-pVDZ(2nd Shell)/PCM | 1.025772 |
| 6-311++G(2d, 2p)(O, H)/cc-pVTZ(Mg, 2nd Shell)/PCM | 1.025919 |

Table 8
Reduced partition function ratios for the brucite cluster using the LC-ωPBE and ωB97XD exchange-correlation functionals at 298.15 K.

| XC/basis set/solvation | $\beta$(RPFR) |
|---|---|
| *LC-ωPBE* | |
| cc-pVTZ(O, H, Mg)/cc-pVDZ(2nd Shell)/PCM | 1.026562 |
| *ωB97XD* | |
| cc-pVTZ(O, H, Mg)/cc-pVDZ(2nd Shell)/PCM | 1.029022 |

become isotopically lighter with increasing temperature (Fig. 5). In contrast to the computations, experiments show that brucite is isotopically light at temperatures below 313.15 K and isotopically heavy at elevated temperature.

## 4. DISCUSSION

The convergence of the RPFR with increasing size of basis set for both the $[Mg(OH_2)_6]^{2+}\cdot 12H_2O$ and for the brucite models agrees well with previous studies (Rustad et al., 2010), and allowed us to select a combination of PBE0 and split-valence triple- and double-zeta basis sets which gives RPFR results that agrees with findings by previous groups (Rustad et al. (2010) and Pinilla et al. (2015)) on the aqueous model. Furthermore, it is important to justify the calculation of RPFRs for solvated ions within the harmonic approximation, as anharmonicity can affect the outcome. Dupuis et al. (2017) find that an anharmonic treatment via path integral molecular dynamics is absolutely necessary for the calculation of isotopic fractionation between Li(I) species. The necessity of calculating fractionations among solvated Li(I) species is crucial because of the variable first hydration shell of Li(I) species. Li(I) exhibits coordination numbers in aqueous solution ranging anywhere from three to six solvating waters (see discussion in Wimpenny et al., 2015). Pinilla et al. (2015) found that calculating RPFRs for solvated Mg(II) via path-integral molecular-dynamic simulations within the harmonic approximation is still valid provided that the disorder of the liquid is considered.

We also found that the size of the brucite cluster did not affect the RPFR, indicating that the termination method is robust. However, the calculations always predict that brucite becomes relatively isotopically lighter as temperatures increase, as the fractionation between brucite and the solvated ion decreases (Fig. 5). Both trends disagree with experimental observations. The experiments show that brucite becomes isotopically heavier with temperature, is isotopically light below 40 °C, and is only isotopically heavy at elevated temperature. While calculating a fractionation factor to accuracy of within one per mil is challenging, predicting the temperature variation of the fractionation factors should be more easily attainable. Here the temperature dependence could only be clearly achieved by fixing the ⟨Mg—O⟩ bond distances in the $[Mg(OH_2)_6]^{2+}\cdot 12H_2O$ model (Fig. 6).

The relative ⟨Mg—O⟩ bond lengths in brucite and in the $[Mg(OH_2)_6]^{2+}$ ion are key to recovering the experimental observation. From crystal structures one expects the Mg (II) aqua ion in solution to be isotopically heavier because the crystals have shorter, stronger ⟨Mg—O⟩ bonds, while brucite should incorporate isotopically lighter Mg, as its ⟨Mg—O⟩ bond distances are greater and thus weaker. The DFT calculations clearly overestimate ⟨Mg—O⟩ bond distances for the $[Mg(OH_2)_6]^{2+}$ ion (see Table 4).

Fixing those bond distances to the values found in epsomite (~2.065 Å) comes much closer to the experimental temperature dependence (Fig. 6). Decreasing the ⟨Mg—O⟩ bond distances even further to 2.050 Å agrees well with the trend of the temperature dependence (Fig. 6). Fig. 6 shows the trend of the fractionation factors over the temperature range 0 to 80 °C as a function of ⟨Mg—O⟩ bond distances in the $[Mg(OH_2)_6]^{2+}\cdot 12H_2O$ complex. This result indicates that it is not entirely necessary to decrease the bond distances to 2.050 Å; rather, the bond distances could be dynamically changing over this temperature range. However, Ohtaki and Radnai (1993), in their comprehensive review, report no strong experimental evidence that

Table 9
Predicted $^{26/24}$Mg isotopic fractionation factors ($\Delta^{26/24}Mg_{solid\text{-}solution}$) at 298.15 K. Positive values indicate the solid is enriched in the heavy isotope. Experiments indicate that it should be negative.

| XC/basis set/solvation | $\Delta^{26/24}Mg_{solid\text{-}solution}$ (‰) |
|---|---|
| *BP86* | |
| 6-31G*(O, H, Mg) | +4.81 |
| 6-31G*(O, H, Mg)/PCM | +5.56 |
| 6-311++G(2d, 2p)(O, H)/6-311G(Mg) | +5.50 |
| 6-311++G(2d, 2p)(O, H)/6-311G(Mg)/PCM | +6.23 |
| *PBE* | |
| 6-311++G(2d, 2p)(O, H)/6-311G(Mg) | +5.37 |
| 6-311++G(2d, 2p)(O, H)/6-311G(Mg)/PCM | +7.21 |
| *B3PW91* | |
| 6-311++G(2d, 2p)(O, H)/6-311G(Mg) | +4.88 |
| 6-311++G(2d, 2p)(O, H)/6-311G(Mg)/PCM | +6.25 |
| *PBE0* | |
| 6-311++G(2d, 2p)(O, H)/6-311G(Mg) | +5.05 |
| 6-311++G(2d, 2p)(O, H)/6-311G(Mg)/PCM | +5.78 |
| cc-pVTZ(O, H, Mg)/cc-pVDZ(2nd Shell)/PCM | +5.62 |
| cc-pVTZ(O, H, Mg)/cc-pVDZ(2nd Shell)/CPCM | +4.48 |
| cc-pVDZ(O, H, Mg)/PCM | +0.86 |
| cc-pVTZ(O, H, Mg)/PCM | +3.14 |
| def2-TZVP(O, H, Mg)/def2-SVP(2nd Shell)/PCM | +3.77 |
| aug-cc-pVTZ(O, H, Mg)/cc-pVDZ(2nd Shell)/PCM | +3.31 |
| aug-cc-pVTZ(O, H)/cc-pVTZ(Mg)/cc-pVDZ(2nd Shell)/PCM | +3.32 |
| 6-311++G(2d, 2p)(O, H)/cc-pVTZ(Mg, 2nd Shell)/PCM | +3.38 |
| *LC-ωPBE* | |
| cc-pVTZ(O, H, Mg)/cc-pVDZ(2nd Shell)/PCM | +3.65 |
| *ωB97XD* | |
| cc-pVTZ(O, H, Mg)/cc-pVDZ(2nd Shell)/PCM | +5.75 |

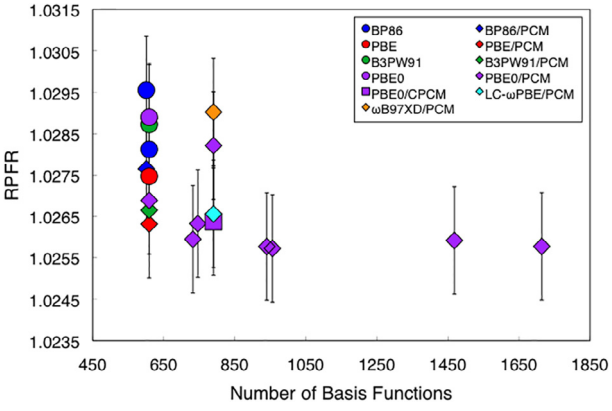


Fig. 4. Convergence of the brucite RPFR as a function of the number of basis functions from various basis set combinations and solvation models used in this study. Error bars indicate one standard deviation of the range. For a list of basis set combinations and corresponding number of basis functions used in this figure, the reader is referred to Tables SI–5.

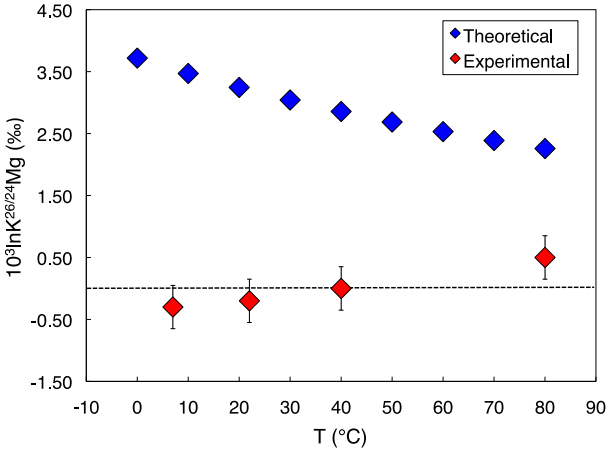


Fig. 5. Predicted isotopic-fractionation factors (blue diamonds) and measured isotopic fractionation factors (red diamonds) between aqueous $[Mg(OH_2)_6]^{2+}$ and brucite. The predicted fractionation factors were computed at PBE0/cc-pVTZ + PCM. The dashed line indicates zero fractionation. (For interpretation of the references to colour in this figure legend, the reader is referred to the web version of this article.)

Mg(II)—$OH_2$ bond distances lengthen over the small temperature range of Li et al. (2014) and Wimpenny et al. (2014).

An important observation is that a temperature dependence similar to the experimental results (Fig. SI-2) could be achieved by leaving the geometry of the $[Mg(OH_2)_6]^{2+}$ cluster equal to that found in the experimental crystal structures. Although if done without geometry optimization, this calculation yielded several imaginary frequency values and is thus considered suspect. However, similar calculations

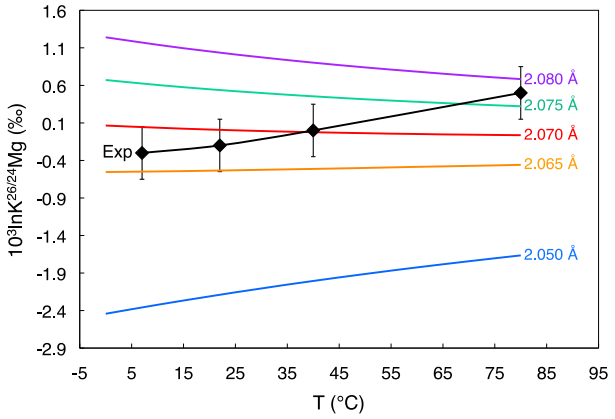


Fig. 6. Fractionation factors for partitioning of magnesium between aqueous $[Mg(OH_2)_6]^{2+}$ ion and brucite optimized at PBE0/cc-pVTZ + PCM, as a function of temperature. The RPFR for the $[Mg(OH_2)_6]^{2+}\cdot 12H_2O$ model was computed as a function of the ⟨Mg—O⟩ bond distance (labeled on plot). The black line and diamonds indicate the experimental work of Wimpenny et al. (2014) and Li et al. (2014).

where geometries were optimized, and thus had no imaginary frequencies, gave a similar result. Specifically, if bond lengths within the $[Mg(OH_2)_6]^{2+}\cdot 12H_2O$ cluster were constrained to be similar to the averaged value found in the minerals (Fig. 6), the experimental temperature dependence is approximately recovered yet without imaginary frequencies because the cluster is optimized. Apparently, the few imaginary frequencies in the fixed-point calculation did not heavily influence the results.

Relaxation of the bulk mineral surface in contact with solution could also affect the isotopic fractionation if the interfacial structure affected the experiments. Wimpenny et al. (2014), for example, attempted to reverse the experiments by diluting the experimental solutions. They attempted to change the saturation state of the solution from one where equilibrium is approached from oversaturation to a state where equilibrium is approached by undersaturation. The new equilibrium would be established by dissolving only a few surface layers from brucite.

Surface relaxation means that bonds change from the bulk values near the immediate interface with another dielectric medium, here the aqueous solution. Such relaxation has been exhibited both experimentally and theoretically in geochemically relevant materials (Rustad et al., 1999; Chambers et al., 2000). The ⟨Mg—O⟩ bond distances in brucite are also observed to increase with increasing temperature (Chakoumakos et al., 1997). While it is clear that ⟨Mg—O⟩ bond lengths in brucite change as a function of temperature, the change in bond length observed by Chakoumakos et al. (1997) at higher temperatures does not coincide with a lighter isotopic signature experimentally, as it should. Theoretically, brucite solid is still enriched in the heavy isotope at high temperatures, but the fractionation decreases and brucite does become lighter (Fig. 5).

If an optimization calculation is allowed to converge without fixed bond lengths, the ⟨Mg—O⟩ bond distances will be consistently overestimated, as found by Rustad et al. (2010) and Schauble (2011). Even when employing the plane-wave methods of Schauble (2011), ⟨Mg—O⟩ bond distances in salts that trap the Mg(II) aqua ion are grossly overestimated, see Table 7 in Schauble (2011) and Table 5 of this study. The most striking disagreement from the work of Schauble (2011) is the $Mg(H_2O)_6Zn_2Br_6$ salt, where the difference between the measured and optimized ⟨Mg—O⟩ bond distance is 0.055 Å. Because of this discrepancy, all salts that trap the Mg(II) aqua ion are not necessarily good models if the bond lengths relax considerably during optimization. The trend of higher RPFRs with shorter bond distances as speculated by Pinilla et al. (2015) is shown in Table 5, where the shortest ⟨Mg—O⟩ bond distance gives the highest RPFR value and the longest bond distance gives the lowest RPFR value, which strongly correlates ⟨Mg—O⟩ bond distance with $^{26}Mg/^{24}Mg$.

One referee asked why fractionation in the magnesite system studied by Rustad et al. (2010) agrees well with experiments. A detailed look at ⟨Mg—O⟩ bond distances in magnesite reveal that magnesite has longer ⟨Mg—O⟩ bond distances than the Mg aqua ion, both theoretically and experimentally. Rustad et al. (2010) calculate values for ⟨Mg—O⟩ bond distances of 2.122 Å for magnesite and 2.096 Å for the Mg(II) aqua ion, and a fractionation of −1.1‰. The negative isotopic excursion, or depletion of heavy isotopes in magnesite, is expected based upon the bond-length analysis.

In recent dissolution experiments of biotite by Ryu et al. (2016), Mg isotopes in biotite are enriched in heavy isotopes, while the leachate is depleted in heavy isotopes. Again, if one looks at the average ⟨Mg—O⟩ bond distances in the trioctahedral layer of biotite, they are 0.012 Å shorter than in brucite and in some cases, the ⟨Mg—O⟩ distance in biotite is as low as 1.997 Å. The most profound result of Ryu et al. (2016) is that Mg isotope temperature dependence at higher temperatures favors the heavy isotope, which agrees well with the experiments of Wimpenny et al. (2014) on brucite.

One additional question arising from the calculations is whether the first hydrolysis product of $[Mg(OH_2)_6]^{2+}$ ion, the $[MgOH(OH_2)_5]^{+}$ ion, also contributes to the isotopic record of growing brucite. If the first hydrolysis product were involved in isotope exchange, it could considerably change the isotopic fractionation, but dynamic simulations would be required to capture the effect. The rate of interconversion of the bound hydroxide and the bound waters within the inner-coordination sphere of the $[MgOH(OH_2)_5]^{+}$ is submillisecond in time scale. These interconversions mean that rapid proton transfer among the bound functional groups would average the bond shortening at the time scale of brucite growth and result in a fractionation factor that changes both with temperature and pH. Such a dynamic process would be difficult to treat realistically using static DFT but would appear naturally in *ab initio* molecular-dynamic simulations.

## 5. CONCLUSIONS

When combined, the experimental results of Li et al. (2014) and Wimpenny et al. (2014) indicate a temperature-dependent reaction where brucite becomes

enriched in heavy magnesium as temperature is increased. Both experimental groups attempted to reverse their experiments and found consistent fractionations upon reversal. The inconsistency provides a clear target for theory and for additional experimentation to examine potential causes.

Although consistent RPFRs could be calculated, using methods of increasing sophistication, the observed temperature variation of isotope fractionation could only be achieved by fixing ⟨Mg—O⟩ bond distances in the aqueous ion to resemble those measured in Tutton's salts that capture the hydrated metal. Electronic-structure calculations with fully optimized models of the hydrated ion, with variable bond lengths, predict brucite being consistently enriched in $^{26}Mg$ at low temperatures, which contrasts with experiment.

Although it is clear that DFT overestimates the ⟨Mg—O⟩ bond distances in aqueous magnesium ions, it is worth pointing out that these fractionations are thermodynamically controlled. Only if exchange between aqueous solutions and brucite were kinetically controlled would fractionations depend on molecular details of the process, such as desolvation rates of $[Mg(OH_2)_6]^{2+}$ ion.

## ACKNOWLEDGEMENTS

The authors are particularly grateful to Dr. James R. Rustad for providing continuous advice and helpful discussions. The authors also thank Dr. Edwin A. Schauble for sharing his plane-wave models of brucite and for providing helpful advice. We are also grateful for the efficient and perceptive editorial handling of the manuscript by associate editor Dr. Fang-Zhen Teng. The manuscript benefited from three very perceptive anonymous reviewers, and we are grateful for their careful reading and excellent suggestions. This work is supported by the U.S. Department of Energy Office of Basic Energy Sciences *via* grant DE-FG02-05ER15693 to WHC. CAO is grateful for a computational allocation (SNIC 2017/3-6) through the Swedish National Infrastructure for Computing.

## APPENDIX A. SUPPLEMENTARY MATERIAL

Supplementary data associated with this article can be found, in the online version, at https://doi.org/10.1016/j.gca.2018.02.005.

## REFERENCES

Adamo C. and Barone V. (1999) Toward reliable density functional methods without adjustable paramters: the PBE0 model. *J. Chem. Phys.* **110**, 6158–6159.

Anbar A. D. and Rouxel O. (2007) Metal isotopes in paleoceanography. *Annu. Rev. Earth Planet. Sci.* **35**, 717–746.

Bauer W. H. (1964) On the crystal chemistry of salt hydrates. IV. The refinement of the crystal structure of $MgSO_4{\cdot}7H_2O$ (epsomite). *Acta Crystallogr.* **17**, 1361–1369.

Becke A. D. (1988) Density-functional exchange-energy approximation with correct asymptotic behavior. *Phys. Rev. A* **38**, 309–3100.

Becke A. D. (1993) Density-functional thermochemistry. III. The role of exact exchange. *J. Chem. Phys.* **98**, 5648–5652.

Bigeleisen J. and Mayer M. G. (1947) Calculation of equilibrium constants for isotopic exchange reactions. *J. Chem. Phys.* **15**, 261–267.

Black J. R., Yin Q.-Y., Rustad J. R. and Casey W. H. (2007) Magnesium isotopic equilibrium in chlorophylls. *J. Am. Chem. Soc.* **129**, 8690–8691.

Chai J.-D. and Head-Gordon M. (2008) Long-range corrected hybrid density functionals with damped atom-atom dispersion corrections. *Phys. Chem. Chem. Phys.* **10**, 6615–6620.

Chakoumakos B. C., Loong C.-K. and Schultz A. J. (1997) Low-temperature structure and dynamics of brucite. *J. Phys. Chem. B* **101**, 9458–9462.

Chambers S. A., Thevuthasan S. and Joyce S. A. (2000) Surface structure of MBE-grown $Fe_3O_4$(001) by X-ray photoelectron diffraction and scanning tunneling microscopy. *Surf. Sci. Let.* **450**, L273–L279.

Colla C. A., Wimpenny J., Yin Q.-Y., Rustad J. R. and Casey W. H. (2013) Calcium-isotope fractionation between solution and solids with six, seven or eight oxygens bound to Ca(II). *Geochim. Cosmochim. Acta* **121**, 363–373.

Dupuis R., Benoit M., Tuckerman M. E. and Méheut M. (2017) Importance of a fully anharmonic treatment of equilibrium isotope fractionation properties of dissolved ionic species as evidenced by $Li^+$(aq). *Acc. Chem. Res.* **50**, 1597–1605.

Frisch M. J., Trucks G. W., Schlegel H. B., Scuseria G. E., Robb M. A., Cheeseman J. R., Scalmani G., Barone V., Mennucci B., Petersson G. A., Nakatsuji H., Caricato M., Li X., Hratchian H. P., Izmaylov A. F., Bloino J., Zheng G., Sonnenberg J. L., Hada M., Ehara M., Toyota K, Fukuda R., Hasegawa J., Ishida M., Nakajima T., Honda Y., Kitao O., Nakai H., Vreven T., Montgomery Jr. J. A., Peralta J. E., Ogliaro F., Bearpark M., Heyd J. J., Brothers E., Kudin K. N., Staroverov V. N., Keith T., Kobayashi R., Normand J., Raghavachari K., Rendell A., Burant J. C., Iyengar S. S., Tomasi J., Cossi M., Rega N., Millam J. M., Klene M., Knox J. E., Cross J. B., Bakken V., Adamo C., Jaramillo J., Gomperts R., Stratmann R. E., Yazyev O., Austin A. J., Cammi R., Pomelli C., Ochterski J. W., Martin R. L., Morokuma K., Zakrzewski V. G., Voth G. A., Salvador P., Dannenberg J. J., Dapprich S., Daniels A. D., Farkas O., Foresman J. B., Ortiz J. V., Cioslowski J., and Fox D. J., Gaussian, Inc., Wallingford CT, 2013.

Immenhauser A., Buhl D., Richter D., Niedermayr A., Riechelmann D., Dietzel M. and Schulte U. (2010) Magnesium-isotope fractionation during low-Mg calcite precipitation in a limestone cave – field study and experiments. *Geochim. Cosmochim. Acta* **74**, 4346–4364.

Klamt A. and Schüürman G. (1993) COSMO: a new approach to dielectric screening in solvents with explicit expressions for the screening energy and its gradient. *J. Chem. Soc. Perkin Trans.* **2**, 799–805.

Li W., Beard B. L., Li C. and Johnson C. M. (2014) Magnesium isotope fractionation between brucite $[Mg(OH)_2]$ and Mg aqueous species: implications for silicate weathering and biogeochemical processes. *Earth Planet. Sci. Lett.* **394**, 82–93.

Mavromatis V., Gautier Q., Bosc O. and Schott J. (2013) Kinetics of Mg partition and Mg stable isotope fractionation during its incorporation in calcite. *Geochim. Cosmochim. Acta* **114**, 188–203.

Ohtaki H. and Radnai T. (1993) Structure and dynamics of hydrated ions. *Chem. Rev.* **93**, 1157–1204.

Papajak E. and Truhlar D. G. (2010) Efficient diffuse basis sets for density functional theory. *J. Chem. Theory Comput.* **6**, 597–601.

Perdew J. P. (1986) Density-functional approximation for the correlation-energy of the inhomogeneous electron-gas. *Phys. Rev. B* **33**, 8822–8824.

Perdew J. P., Burke K. and Ernzerhof M. (1996a) Generalized gradient approximation made simple. *Phys. Rev. Lett.* **77**, 3865–3868.

Perdew J. P., Ernzerhof M. and Burke K. (1996b) Rationale for mixing exact exchange with density functional approximations. *J. Chem. Phys.* **105**, 9982–9985.

Pinilla C., Blanchard M., Balan E., Natarajan S. K., Vuilleumier R. and Mauri F. (2015) Equilibrium magnesium isotope fractionation between aqueous $Mg^{2+}$ and carbonate minerals: insights from path integral molecular dynamics. *Geochim. Cosmochim. Acta* **163**, 126–139.

Richens D. T. (1997) *The Chemistry of Aqua Ions*. John Wiley & Sons, New York.

Rustad J. R., Wasserman E. and Felmy A. R. (1999) A molecular dynamics investigation of surface reconstruction on magnetite (001). *Surf. Sci.* **432**, L583–L588.

Rustad J. R., Nelmes S. L., Jackson V. E. and Dixon D. A. (2008) Quantum-chemical calculations of carbon-isotope fractionation in $CO_2$(g), aqueous carbonate species, and carbonate minerals. *J. Phys. Chem. A* **112**, 542–555.

Rustad J. R. and Dixon D. A. (2009) Prediction of iron-isotope fractionation between hematite ($\alpha$-$Fe_2O_3$) and ferric and ferrous iron in aqueous solution from density functional theory. *J. Phys. Chem. A* **113**, 12249–12255.

Rustad J. R., Casey W. H., Yin Q.-Y., Bylaska E. J., Felmy A. R., Bogatko S. A., Jackson V. E. and Dixon D. A. (2010) Isotopic fractionation of $Mg^{2+}$(aq), $Ca^{2+}$(aq), and $Fe^{2+}$(aq) with carbonate minerals. *Geochim. Cosmochim. Acta* **74**, 6301–6323.

Ryu J.-S., Vigier N., Decarreau A., Lee S.-W., Lee K.-S., Song H. and Petit S. (2016) Experimental investigation of Mg isotope fractionation during mineral dissolution and clay formation. *Chem. Geol.* **445**, 135–145.

Schauble E. A., Méheut M. and Hill P. S. (2009) Combining metal stable isotope fractionation theory with experiments. *Elements* **5**, 369–374.

Schauble E. A. (2011) First-principles estimates of equilibrium magnesium isotope fractionation in silicate, oxide, carbonate and hexaaquamagnesium(2+) crystals. *Geochim. Cosmochim. Acta* **75**, 844–869.

Schott J., Mavromatis V., Fuji T., Pearce C. R. and Oelkers E. H. (2016) The control of carbonate mineral Mg isotope composition by aqueous speciation: theoretical and experimental modeling. *Chem. Geol.* **445**, 120–134.

Tomasi J., Mennucci B. and Cammi R. (2005) Quantum mechanical continuum solvation models. *Chem. Rev.* **105**, 2999–3093.

Urey H. C. (1947) The thermodynamic properties of isotopic substances. *J. Chem. Soc.*, 562–581.

Vydrov O. A. and Scuseria G. E. (2006) Assessment of a long-range corrected hybrid functional. *J. Chem. Phys.* **125**, 234109.

Wimpenny J., Colla C. A., Yin Q.-Z., Rustad J. R. and Casey W. H. (2014) Investigating the behavior of Mg isotopes during the formation of clay minerals. *Geochim. Cosmochim. Acta* **128**, 178–194.

Wimpenny J., Colla C. A., Yu P., Yin Q.-Z., Rustad J. R. and Casey W. H. (2015) Lithium isotope fractionation during uptake by gibbsite. *Geochim. Cosmochim. Acta* **168**, 133–150.

Wu Z., Huang F. and Huang S. (2015) Isotope fractionation induced by phase transformations: first-principles investigation for $Mg_2SiO_4$. *Earth Planet. Sci. Lett.* **409**, 339–347.

Young E. D., Manning C. E., Schauble E. A., Shahar A., Macris C. A., Lazar C. and Jordan M. (2015) High-temperature equilibrium isotope fractionation of non-traditional stable isotopes: experiments, theory, and applications. *Chem. Geol.* **395**, 176–195.

Zigan F. and Rothbauer R. (1967) Neutron diffraction measurements of brucite. *Neues Jahrbuch fuer Mineralogie. Monatshefte.* **4–5**, 137–143.

*Associate editor:* Fang-Zhen Teng